

Preserving Porosity of Mesoporous Metal–Organic Frameworks through the Introduction of Polymer Guests

Li Peng,^{†,#} Shuliang Yang,^{†,#} Sudi Jawahery,^{‡,§} Seyed Mohamad Moosavi,^{⊥,§} Aron J. Huckaba,[†] Mehrdad Asgari,[†] Emad Oveisi,[§] Mohammad Khaja Nazeeruddin,^{†,§} Berend Smit,^{⊥,‡,§} and Wendy L. Queen^{*,†,§}

[†]Institute of Chemical Sciences and Engineering, École Polytechnique Fédérale de Lausanne (EPFL), Rue de l'Industrie 17, CH-1951 Sion, Switzerland

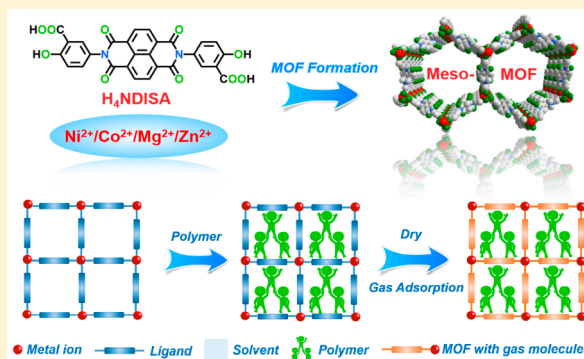
[⊥]Laboratory of Molecular Simulation (LSMO), Institut des Sciences et Ingénierie Chimiques, Valais, Ecole Polytechnique Fédérale de Lausanne (EPFL), Rue de l'Industrie 17, CH-1951 Sion, Switzerland

[‡]Department of Chemical and Biomolecular Engineering, University of California, Berkeley, Berkeley, California 94720, United States

[§]Interdisciplinary Center for Electron Microscopy, École Polytechnique Fédérale de Lausanne (EPFL), CH-1015 Lausanne, Switzerland

Supporting Information

ABSTRACT: High internal surface areas, an asset that is highly sought after in material design, has brought metal–organic frameworks (MOFs) to the forefront of materials research. In fact, a major focus in the field is on creating innovative ways to maximize MOF surface areas. Despite this, large-pore MOFs, particularly those with mesopores, continue to face problems with pore collapse upon activation. Herein, we demonstrate an easy method to inhibit this problem via the introduction of small quantities of polymer. For several mesoporous, isostructural MOFs, known as $M_2(\text{NDISA})$ (where $M = \text{Ni}^{2+}$, Co^{2+} , Mg^{2+} , or Zn^{2+}), the accessible surface areas are increased dramatically, from 5 to 50 times, as the polymer effectively pins the MOFs open. Postpolymerization, the high surface areas and crystallinity are now readily maintained after heating the materials to 150 °C under vacuum. These activation conditions, which could not previously be attained due to pore collapse, also provide accessibility to high densities of open metal coordination sites. Molecular simulations are used to provide insight into the origin of instability of the $M_2(\text{NDISA})$ series and to propose a potential mechanism for how the polymers immobilize the linkers, improving framework stability. Last, we demonstrate that the resulting MOF–polymer composites, referred to as $M_2(\text{NDISA})\text{-PDA}$, offer a perfect platform for the appendage/immobilization of small nanocrystals inside rendering high-performance catalysts. After decorating one of the composites with Pd (average size: 2 nm) nanocrystals, the material shows outstanding catalytic activity for Suzuki–Miyaura cross-coupling reactions.



INTRODUCTION

High porosity, an attribute that promotes the adsorption of large quantities of guest species and their rapid diffusion in and out of materials, has quickly brought metal–organic frameworks (MOFs) to the forefront of material science research efforts.^{1–3} These porous, crystalline frameworks offer unprecedented internal surface areas up to 7800 m²/g,⁴ and due to their modular design, the internal MOF surfaces can be readily decorated with a wide range of chemical moieties, allowing one to selectively adsorb a targeted analyte.^{5–8} These properties make MOFs of interest in a wide array of applications coupled to sensing, drug delivery, catalysis, separation, storage, etc.^{9–12} Unfortunately, to date, most reported MOFs are microporous (with pore diameters < 2

nm), limiting their use in several practical applications such as catalysis and capture of large molecules. Large mesoporous networks (with pore apertures > 2 nm) can not only offer higher internal surface area and pore volumes but also allow the inclusion of a broader range of guest species, all while promoting faster mass transfer. As such, there are several developed methodologies for the synthesis of MOFs with large pores,^{13–18} such as the elongation of the organic linkers.^{19–23} However, many existing large-pore networks lose significant amounts of accessible surface area during solvent removal/exchange.^{24–27} The interactions between the solvent and the

Received: June 4, 2019

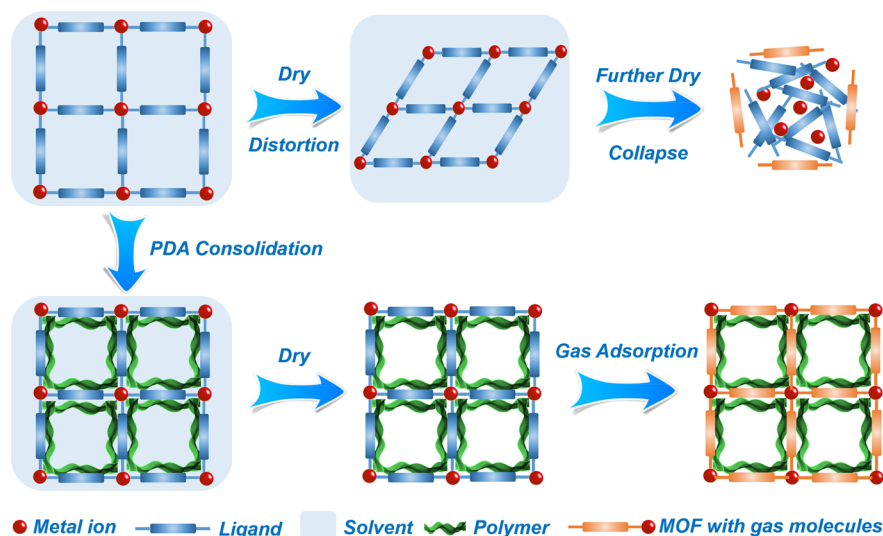


Figure 1. Polymer introduced into the pore channel supports the porous structure and prevents the mesopores from collapsing, leaving the pores accessible to gas molecules.

MOF walls can help stabilize the framework; however, the removal of solvent molecules puts stress on the heavy framework struts, distorting the MOF structure, and eventually resulting in pore collapse (Figure 1).²⁸

The specific chemistry of a given MOF is likely important in determining the extent to which a given framework will be prone to collapse upon activation. For instance, it has been shown that decorating the linkers of otherwise isostructural ZIFs with organic functional groups impacts their mechanical properties.²⁹ Also, in a recent study, the mechanical properties of $M_2(\text{dobdc})$ (where $M = \text{Co}^{2+}$, Fe^{2+} , Mg^{2+} , Mn^{2+} , Ni^{2+} , and Zn^{2+}) and an expanded, isorecticular analogue were computed and compared. The expanded analogues were consistently less rigid than $M_2(\text{dobdc})$ across the whole series of metals studied. This suggests that, in addition to the stress induced by the evaporation of polar solvent clusters from the large-pore apertures,³⁰ large-pore MOFs may be inherently more susceptible to collapse because of their decreased rigidity. While mild activation procedures,^{24,25} such as supercritical CO_2 drying, have been developed for the activation of large-pore MOFs, this process can be quite time- and labor-intensive. Further, the method is not always effective,^{28,31–33} particularly for MOFs having solvent that is bound to metals. The presence of open metal coordination sites (OMCs), more often than not, requires high-temperature, vacuum-based activation to liberate solvent molecules from OMCs. In addition, without the solvent, some MOFs, such as Zn-HKUST-1, SDU-1, and the Cd-based MOF IFP-6, are most likely unstable; this implies that for such materials any attempt to find a better activation process is doomed to fail.^{34–37}

An example of a mesoporous MOF with collapsible pores was recently synthesized by Dincă et al. This material is referred to as $M_2(\text{NDISA})$ (where $M = \text{Mg}^{2+}$ and Ni^{2+}). The Ni^{2+} analogue, which required supercritical CO_2 drying for activation,²⁰ has a reported Brunauer–Emmett–Teller (BET) surface area of $\sim 1722 \text{ m}^2/\text{g}$. This value is well below the theoretical surface area ($2872 \text{ m}^2/\text{g}$, determined using Zeo++ for a probe radii of 1.860 \AA).³⁸ Further, the structure of the Mg^{2+} analogue reportedly undergoes a complete pore collapse even after a mild activation with supercritical CO_2 .

Inspired by previous work on $M_2(\text{NDISA})$, we hypothesized that inserting polymer guests into this material could pin the mesopore open and also enhance the mechanical stability of the framework, maintaining porosity even upon harsh activation conditions. It should be noted that integrating polymers and MOFs is an emerging topic in the field.^{39,40} Nonetheless, to date, there are no reports showing methods that are capable of maintaining the structural integrity of mesoporous MOFs during activation. However, there has been some recent works in the literature that demonstrate that the insertion of polymer guests can enhance mechanical stability and decrease flexibility in microporous MOFs.^{41,42}

In this work, we pursued the development of a new, facile method for preserving the porosity of mesoporous MOFs through the incorporation of small quantities of polymer guests into the host framework (Figure 1). In addition, we have used molecular simulations to investigate the underlying mechanism behind the instability of $M_2(\text{NDISA})$. Experimentally we show a significant enhancement in MOF surface areas upon polymer insertion compared to the activated MOFs without any polymer, where the surface areas improve by factors ranging from 5 to 50. We were also able to synthesize two new crystalline analogues, including $\text{Co}_2(\text{NDISA})$ and $\text{Zn}_2(\text{NDISA})$, which were previously inaccessible due to pore collapse during solvent exchange/evaporation. The new MOF–polymer composites can now withstand harsh activation conditions that allow access to large quantities of OMCs. Our simulations show that intermolecular interactions between functional groups present on the NDISA ligand result in a large torque on the metal helices, destabilizing the MOFs. Lastly, we demonstrate that the MOF–polymer composites are suitable to incorporate small, homogeneous nanocrystals, provoking thought toward using the mesoporous composites as a platform for the design of a variety of new catalytic systems.

RESULTS AND DISCUSSION

Strategy and Characterizations. Using $M_2(\text{NDISA})$ as a proof of concept material, we first developed a synthetic protocol for the organic linker, naphthalene diimide salicylic acid (NDISA), and then determined the reaction conditions necessary to isolate a series of isostructural $M_2(\text{NDISA})$

MOFs, where $M = \text{Mg}^{2+}$, Co^{2+} , Ni^{2+} , or Zn^{2+} . The resulting $M_2(\text{NDISA})$ structure consists of metal oxide chains that are interlinked by the NDISA ligands, forming one-dimensional channels with a pore diameter of >3.0 nm (Figure 2).²⁰ The M^{2+} ions are octahedrally coordinated, with solvent molecules that are bound in one of the apical positions and point directly into the framework channel.

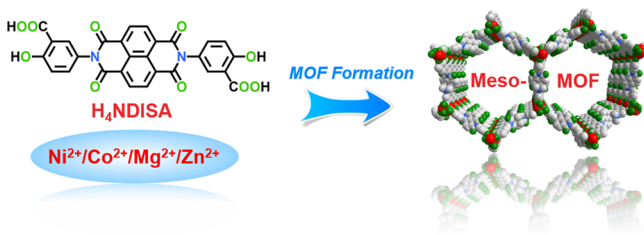


Figure 2. Metal ions, ligand for MOF synthesis, and the MOF structure. Atom colors: metal ions, red; C, gray; O, green; N, cyan; H atoms were omitted for clarity.

Postsynthesis, the $M_2(\text{NDISA})$ frameworks underwent solvent exchange with methanol and subsequent activation at 150 °C for 12 h (under vacuum). The chosen activation conditions are those able to liberate the solvent molecules from the metal ions.²⁸ For $\text{Ni}_2(\text{NDISA})$, subsequent N_2 adsorption measurements taken at 77 K indicate a modest BET surface area (SA) of only 433 m^2/g . The low internal surface areas prompted us to look for an effective method to preserve the porosity of this mesoporous MOF. Recently, we discovered that free-base dopamine monomers can spontaneously polymerize inside MIL-100 (Fe-BTC), which has open iron coordination sites that drive the anaerobic oxidation process.⁴³ Given that $\text{Ni}_2(\text{NDISA})$ has Ni^{2+} ions embedded in the framework wall, we deduced that the postsynthetic introduction of free-base dopamine monomers, followed by subsequent polymerization to polydopamine (PDA), might act as the pillars and pin the large-pore MOF open during a subsequent activation. As such, *in situ* polymerization was carried out inside $\text{Ni}_2(\text{NDISA})$, and scanning electron microscope (SEM) and transmission electron microscope (TEM) images of $\text{Ni}_2(\text{NDISA})$ and $\text{Ni}_2(\text{NDISA})\text{-PDA}$ show no obvious difference in the overall crystal morphology (Figure S1). However, TEM images show evidence of mesopore channels for $\text{Ni}_2(\text{NDISA})\text{-PDA}$ (Figure S2). For $\text{Ni}_2(\text{NDISA})\text{-PDA}$, loaded with only 6.8 wt % PDA, the BET SA increases dramatically to 2276 m^2/g . This value is 5 times the surface area of the parent structure treated under the same conditions and is significantly closer to the theoretical surface area of 2872 m^2/g . It is noted that, despite the presence of the polymer, the surface area that we achieved is also significantly higher than that reported by Dincă et al.: 1722 m^2/g using supercritical CO_2 drying.²⁰

For $\text{Mg}_2(\text{NDISA})$, there is negligible accessible surface area due to a total framework collapse (Figure 3a). Likewise, the two newly synthesized analogues, including $\text{Co}_2(\text{NDISA})$ and $\text{Zn}_2(\text{NDISA})$, are found to undergo a phase change immediately after solvent exchange, implying that even this process is too harsh to sustain the mesoporous structure (Figure S3). As such, postsynthetic polymerization was also carried out on the three additional analogues. The resulting composites, $\text{Zn}_2(\text{NDISA})\text{-PDA}$, $\text{Co}_2(\text{NDISA})\text{-PDA}$, and $\text{Mg}_2(\text{NDISA})\text{-PDA}$, have BET SAs of 402, 1756, and 753 m^2/g ; these are 20, 24, and 50 times that of the parent

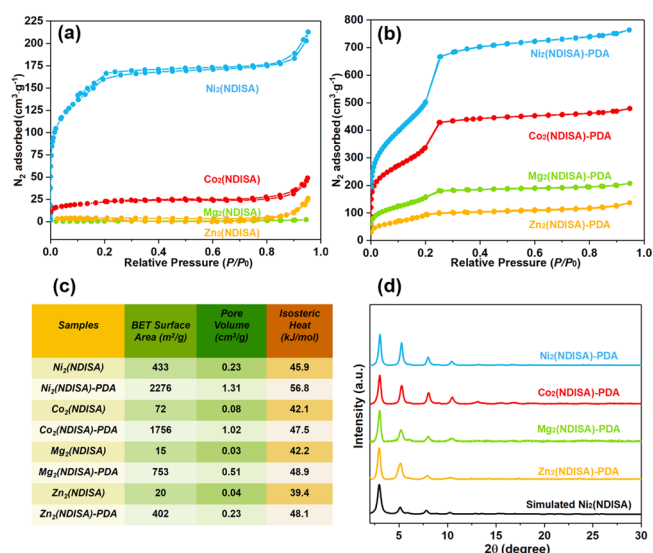


Figure 3. (a) N_2 adsorption isotherms of MOFs; (b) N_2 adsorption isotherms of MOF-PDA samples; (c) BET surface areas, pore volume, isosteric heat of MOFs and MOF-PDA samples; (d) XRD patterns of the MOF-PDA samples.

materials treated under the same reaction conditions, respectively. Other than the Ni analogue, the BET SAs of the parent structures indicate almost total pore collapse when activated at 150 °C (Figure 3a and c).

The amount of polymer loaded in the pores was determined indirectly using inductively coupled plasma optical emission spectrometry (ICP-OES). The PDA loadings of $\text{Ni}_2(\text{NDISA})\text{-PDA}$, $\text{Co}_2(\text{NDISA})\text{-PDA}$, $\text{Mg}_2(\text{NDISA})\text{-PDA}$, and $\text{Zn}_2(\text{NDISA})\text{-PDA}$ are estimated to be 6.8, 5.3, 5.8, and 2.4 wt %, respectively. Furthermore, these data were cross-checked using thermal gravimetric analysis (TGA), which suggests that the PDA contents in the samples are 7.0, 6.7, 6.9, and 2.7 wt %, respectively (Figure S4 and Table S1). These values are comparable to the ICP-OES results, and slight differences are likely due to minor variations in the solvation level of the tested samples.

We also conducted a series of experiments to study the effects that different polymer concentrations have on the BET surface areas. The results are shown in Table S2 and Figure S5. It is noted that the SAs of $\text{Co}_2(\text{NDISA})\text{-PDA}$, $\text{Mg}_2(\text{NDISA})\text{-PDA}$, and $\text{Zn}_2(\text{NDISA})\text{-PDA}$ are significantly lower than the theoretical surface area, regardless of the polymer loading. This is likely due to crystalline defects formed during crystal growth or the presence of amorphous gels that cannot be detected via powder X-ray diffraction. Despite this, the polymer composites have 5 to 50 times larger BET SAs than those of the parent structures treated under the same activation conditions. Further, the X-ray diffraction (XRD) patterns of $\text{Ni}_2(\text{NDISA})\text{-PDA}$, $\text{Co}_2(\text{NDISA})\text{-PDA}$, $\text{Mg}_2(\text{NDISA})\text{-PDA}$, and $\text{Zn}_2(\text{NDISA})\text{-PDA}$ well match the simulated PXRD pattern of $\text{Ni}_2(\text{NDISA})$, indicating that the materials are isostructural after the polymer insertion and activation (Figure 3d). Subsequent Le Bail refinement performed on the collected powder diffraction patterns of the composite samples further confirms the integrity of the crystalline structure and the isostructural nature of the frameworks (Figure S6).

Furthermore, *in situ* diffuse reflectance infrared Fourier transform spectroscopy (*in situ* DRIFTS) was used to probe both $\text{Ni}_2(\text{NDISA})$ and $\text{Ni}_2(\text{NDISA})\text{-PDA}$ for open Ni(II) sites

postactivation. Both samples were first heated to 150 °C under vacuum for 12 h to remove solvent molecules. Each sample was placed under 9.6 mbar of CO, and then the diffuse reflectance spectra were collected. Each spectrum reveals peaks characteristic of Ni(II)-bound CO at $\sim 2175\text{ cm}^{-1}$, a value that is significantly shifted from the expected stretching frequency of free CO, 2143 cm^{-1} (Figure S7).^{44,45} Under the same test condition, the intensity of the characteristic peak derived from Ni₂(NDISA)-PDA is much stronger than that of Ni₂(NDISA); this implies accessibility to a larger number of metal sites and that the polymerization process is not blocking all of the OMCs. A similar phenomenon is observed for Co₂(NDISA)-PDA, Mg₂(NDISA)-PDA, and Zn₂(NDISA)-PDA (Figures S8–S10). This result confirms that the PDA supports the porous structure all while effectively increasing the availability of OMCs. The presence of high densities of reactive, electron-deficient OMCs can reportedly enhance framework selectivity, improve the surface packing density of adsorbates, and provide reactive sites to facilitate gas phase reactions on the internal MOF surface.^{46–49}

Molecular Simulation. In order to better understand the physical origins of the structural collapse of M₂(NDISA), we used a recently developed model for M₂(dobdc) analogues to perform simulations of the framework.⁵⁰ This model was previously tested successfully on a series of isorecticular M₂(dobdc) analogues that are known to be stable upon activation. This series included IRMOF-74-V, which has a structure similar to M₂(NDISA), but slightly larger pores (38 Å).⁵¹

To test the stability of M₂(NDISA) structures, we performed molecular dynamics (MD) simulations on the M₂(NDISA) structures after removing the solvents. The M₂(NDISA) structures underwent large deformations in the MD simulations (see Figure S11 for snapshots). The π - π stacking interactions between the naphthalene groups on adjacent ligands apply an attractive force between the ligands such that the center of ligands approach each other and stack in the direction of the one-dimensional channels (see Figure S12). This reorganization propagates a change of orientation of the salicylic acid groups with respect to the metal helix axis and causes significant deformation of the metal helices, in some cases leading to a dramatic collapse of the pore.

This observation suggests that the specific π - π interactions cause a stacking of the linkers of M₂(NDISA), which results in a force on the metal helices. This force leads to their structural collapse. To quantify this effect, we computed the forces applied by the ligand on the metal helix at the points of attachment: the coordinating ligand oxygens. For this analysis, the metal helix is treated as a rigid body and the positions of the metals are kept fixed during the MD simulation. Figure 4a and b show that indeed the NDISA ligands impose a large force on the metal rods when compared to the ligands in the stable IRMOF-74-V system. Since these forces are not aligned with the helix–oxygen vector, they impose a net torque on the metal rods, which causes the structural deformation and even pore collapse. The total linker force vectors for all M₂(NDISA) analogues are shown in Figure S13, and the force components contributing to the torque are shown in Figure S14. We summarize the magnitude of the torques in different systems in Figure 4c. Since the metal rods are relatively rigid, they can withstand some local stress (e.g., IRMOF-74-V) that exists and the forces and torques imposed on them, but our calculations

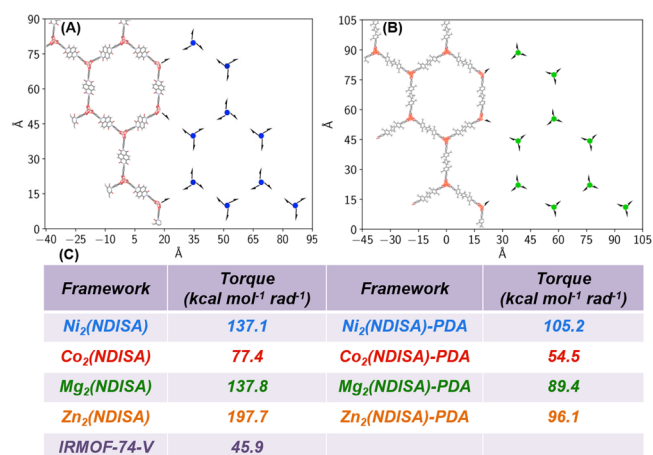


Figure 4. (a) Total force applied by linkers on metal helices in a Ni₂(NDISA) system simulated at 300 K; (b) total force applied by linkers in metal helices in an IRMOF-74-V system simulated at 300 K; (c) average helix torque in simulated MOF and MOF-PDA systems at 300 K. In both (a) and (b), the magnitude of the force (kcal mol⁻¹ Å⁻¹) is related to the tick mark values, scaled by a factor of 0.02.

suggest that in the M₂(NDISA) systems this torque is too large for the helix to tolerate.

It is interesting to investigate whether the introduction of polymers into M₂(NDISA) could change the force and torque that the ligands exert on the metal helices. Here we propose a possible mechanism for how polymers may affect the force and torque. Assuming that the polymers are located at the open metal sites, we employ a harmonic bond between the dopamine nitrogen and the metal to mimic the strong interaction between these atoms. It is important to note that experimentally the polymer has as many as five monomer units (Figure S15), compared with the simulation, which has only one. Additionally, although binding to the open metal sites is expected considering the Lewis base functionality on the PDA backbone, we have not yet elucidated the nature of the PDA coordination experimentally, making a direct comparison between the theoretical and experimental results difficult. For the simulations, three different ratios of dopamine:M₂(NDISA) were used. These ratios include 2:9, 4:9, and 6:9 (Figures S16–S18). Figure 4c also reports the magnitude of torque on the metal helices computed from the M₂(NDISA) simulations at a dopamine to open metal site ratio of 6:9; this was the largest concentration of monomers that fit on the open metal sites such that dopamine molecules did not overlap. A comparison between average torques for systems with and without dopamine shows that the dopamine can immobilize the linkers and decrease the torque on the metal helices (Figure 4c and Figures S18 and S19).

CO₂ Adsorption. Given the higher number of OMCs and nitrogen-containing polymers, we probed the CO₂ adsorption properties of the activated parent structures as well as their corresponding composites. The CO₂ adsorption properties of Ni₂(NDISA) and Ni₂(NDISA)-PDA were probed at 298 K to check the accessibility of CO₂ molecules before and after the polymer loadings. Figure S20 shows the room-temperature CO₂ adsorption isotherms for Ni₂(NDISA) and Ni₂(NDISA)-PDA. The capacity of Ni₂(NDISA) for CO₂ adsorption at approximately 1.2 bar is 0.97 mmol/g; however after loading PDA, the capacity of Ni₂(NDISA)-PDA reached 2.87 mmol/g, which is 3 times that of the sample without PDA struts.

Additionally, the CO₂ adsorption isotherms collected at 278, 293, and 308 K were fitted with a dual-site Langmuir model, and isosteric heat was extracted from the variable-temperature CO₂ adsorption (Figures S21 and S22). The isosteric heats of adsorption (Q_{st}) for Ni₂(NDISA) and Ni₂(NDISA)-PDA are 45.9 and 56.8 kJ/mol, respectively (Figure S21). The higher isosteric heat for Ni₂(NDISA)-PDA could result from the significantly larger number of OMCs, as predicted based on the Boltzmann distribution,^{6,52} as well as the inclusion of the amine-containing polymer, which is known to offer strong adsorption sites for CO₂.^{53–55} This phenomenon is also observed for other samples, Co₂(NDISA)-PDA, Mg₂(NDISA)-PDA, and Zn₂(NDISA)-PDA (Figures S23–S25 and Table S3). These results indicate the introduced polymers play a pivotal role in enhancing surface area and CO₂ adsorption performance.

Extension of the Current Strategy. We also extended the investigation to determine if the postsynthetic insertion of preformed polymers might also enhance surface areas. Polyethylenimine (PEI) with a low molecular weight was employed in order to promote the diffusion of the polymer into the materials. Branched PEI with a molecular weight of 600 was added into the methanol solution and mixed with the as-prepared MOFs. According to the ICP-OES results, the PEI loadings are 8.8, 12.8, 14.9, and 11.9 wt % for Ni₂(NDISA)-PEI, Co₂(NDISA)-PEI, Mg₂(NDISA)-PEI, and Zn₂(NDISA)-PEI, respectively. The resulting XRD patterns are similar to those of the simulated XRD pattern of Ni₂(NDISA) (Figure S26a). Similar to MOFs with PDA pillars, the BET surface areas of M₂(NDISA)/PEI composites activated at 110 °C are 1803, 1480, 1023, and 743 m²/g for Ni²⁺, Co²⁺, Mg²⁺, and Zn²⁺, respectively (Figure S26b). These surface areas are increased by a factor of 4 to 68 compared to the parent M₂(NDISA) structure activated under the same conditions. These results confirm that postsynthetic insertion of low-molecular-weight polymers can also prevent the mesoporous MOF from collapsing during harsh activation procedures.

Application for Catalysis. This method endows M₂(NDISA) with high internal surface areas and hence maintains large pore volumes and diameters, as shown by the pore size distribution (Figures S27–S30). Therefore, it was thought that these MOF–polymer composites might offer a perfect platform for the immobilization of nanoparticles (NPs) for catalysis. On one hand, the reinforced mesoporous structure allows improved molecular accessibility and thus can improve mass transfer;¹⁷ on another hand, the redox-active PDA has metal scavenging and reducing functionality that can immobilize NPs for catalysis.⁴³ With this in mind, Pd NPs were first loaded into Ni₂(NDISA)-PDA, as it shows the highest surface area among the four MOF composites. SEM images showed that the synthesized sample (denoted as Ni₂(NDISA)-PDA-Pd) displays a spherical morphology assembled by nanorods (Figure 5a). TEM images confirmed that Pd NPs, with an average size of ~2 nm, are uniformly dispersed in the nanorods. It is likely that the polymer inhibits Pd aggregation during the preparation process (Figure 5b–e), resulting in Pd nanoparticles with small sizes. ICP-OES analysis revealed that the Pd loading in Ni₂(NDISA)-PDA-Pd was ~3.36 wt %, and X-ray photoelectron spectroscopy (XPS) analysis confirmed that the Pd NPs consist of metallic Pd and ionic Pd(II) (Figure S31). The presence of Pd(II) is likely due to the partial oxidation from the air exposure. The XRD pattern of Ni₂(NDISA)-PDA-Pd is similar to the one obtained from

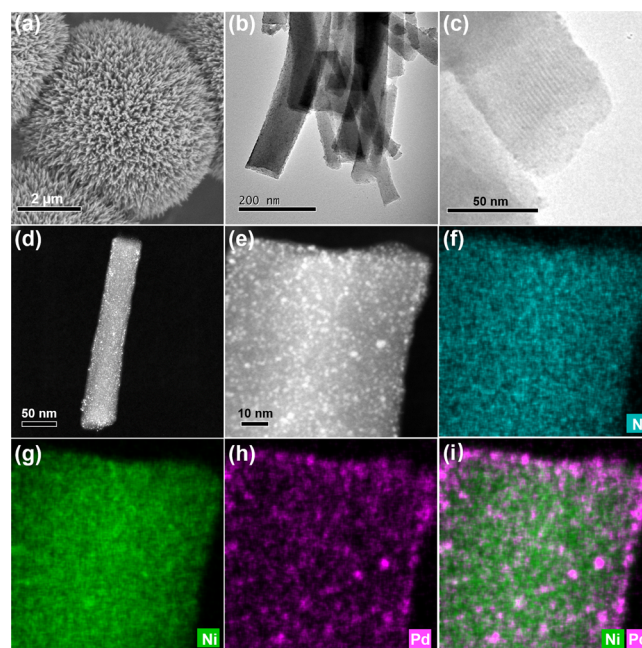
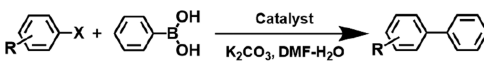


Figure 5. SEM image (a), bright-field TEM images (b, c), HAADF-STEM images (d, e), and corresponding EDX elemental maps of N (f), Ni (h), Pd (h), and overlapped (i) Ni and Pd of Ni₂(NDISA)-PDA-Pd.

Ni₂(NDISA)-PDA. No obvious peaks related to metallic Pd are observed (Figure S32), a result of the very small Pd NPs observed in the TEM. Further, Ni₂(NDISA)-PDA-Pd had a BET surface area of 1681 m²/g, which is only slightly less than the parent Ni₂(NDISA)-PDA (1989 m²/g for a 15.7 wt % PDA loading) (Figure S33). This implies that the pore channels are not blocked after loading the NPs. Previous reports show more significant decreases in surface areas when mesoporous MOFs are used as supports for metal NPs.^{56–59} This is often the case even when the amount of loaded NPs is significantly lower than the one used in this study. The final Pd loading can also be controlled by tuning the reaction time and the amount of introduced Pd(NO₃)₂ precursor (Table S4 and Figure S34).

Next, because the Ni₂(NDISA)-PDA-Pd composite combines the benefits of a mesoporous structure with well-dispersed, ultrasmall NPs, we chose to demonstrate its use as a catalyst for Suzuki coupling reactions. As shown in Table 1, phenylboronic acid was coupled with various aryl iodides and aryl bromides, providing satisfying yields with only an ultralow 0.1 mol % Pd loading. For 4-iodotoluene, Ni₂(NDISA)-PDA-Pd affords a 48% yield in 5 min with a TOF (defined as moles of 4-iodotoluene converted per mol of Pd per hour) as high as 5760 h⁻¹. We should point out that this catalytic performance is very impressive, even besting the state-of-the-art homogeneous Pd(PPh₃)₂Cl₂ catalyst.⁶⁰ As control experiments, we tested the performance of Ni₂(NDISA) and PDA-Pd. The results show that Ni₂(NDISA) has no activity for the reaction (entry 5) and PDA-Pd gave a yield of only 3% in 3 h (entry 6) due to the very low accessible surface area (7 m²/g, Figure S35). We also used the Ni₂(NDISA) (BET surface area: 433 m²/g, Figure 3a) as a support for Pd NPs and tested the performance as a control experiment. The Ni₂(NDISA)-Pd required 3 h to reach a yield of 83%, whereas Ni₂(NDISA)-PDA-Pd required only 1 h to obtain the same yield (entries 4 and 7). Further, the TEM images of Ni₂(NDISA)-Pd (3.82 wt

Table 1. Suzuki Coupling Reactions with Varied Catalysts^a


Entry	Aryl halides	τ (h)	Yield (%)
1		3	>99
2		1	97
3 ^b		2	96
4		1 3	83 90
5 ^c		3	n.d.
6 ^d		3	3
7 ^b		3	83
8		1	>99
9		3	48
10		3	96

^aReaction conditions: aryl halide (1 mmol), phenylboronic acid (1.1 mmol), K_2CO_3 (1.5 mmol), $Ni_2(NDISA)$ -PDA (0.1 mol % Pd), DMF- H_2O (3 mL, $V_{DMF}:V_{H_2O} = 1:1$), 50 °C. ^b $Ni_2(NDISA)$ -Pd as catalyst. ^c $Ni_2(NDISA)$ as catalyst. ^dPDA-Pd as catalyst.

% Pd) show that the Pd NPs have a nonuniform size distribution ranging from 2 to 7 nm (Figure S36). The outstanding performance of $Ni_2(NDISA)$ -PDA-Pd catalyst is therefore ascribed to the following potential reasons: (1) The higher pore volume and surface area offered by the Pd-supported $Ni_2(NDISA)$ -PDA composite improves mass transfer inside the MOF channels, a problem from which most microporous MOF catalysts suffer;^{61,62} (2) the high density of coordinating functional groups on the PDA backbone promotes the formation of ultrasmall, well-dispersed, and uniform Pd nanoclusters, which provide more active sites when compared to the larger Pd NPs;⁶³ (3) PDA in the composite, which can also act as a reducing agent, endows the Pd clusters with very clean surfaces; the use of surfactants and stabilizers, often adopted to prepare small NPs, was avoided in this case.^{64,65} We should point out that the Suzuki coupling reaction, which is heated in the presence of base, gives rise to the slow decomposition of the MOF support (Figures S37–S39). Until now, this stability issue is still one of the main problems facing MOF use in this reaction, and effort is underway in our laboratory to further stabilize the catalyst.^{30,66}

CONCLUSIONS

This is the first report showing that the insertion of small quantities of polymers into MOF structures is a tool that can be used to inhibit the collapse of mesoporous frameworks. An isostructural family of MOFs, known as $M_2(NDISA)$ where $M = Ni, Co, Mg, \text{ and } Zn$, was synthesized and subsequently activated under harsh conditions, including high heat (150 °C) and vacuum. While many of the MOFs in this family show limited to no surface areas postactivation, the MOF–polymer composites show BET surface areas that are improved by factors ranging from 5 to 50 times that of the parent material. Using this method, we are also able to isolate two new analogues, $Co_2(NDISA)$ and $Zn_2(NDISA)$, whose structures were previously inaccessible due to their strong susceptibility

to pore collapse during solvent exchange/evaporation. We have investigated the mechanism of collapse via molecular simulations and determined that strong intermolecular interactions between linkers destabilize the metal helices that act as mechanical struts. It is thought that this method for polymer-induced stabilization can be easily extended to a number of other mesoporous MOFs. In addition, the resulting MOF–polymer composites are an excellent platform for the design of new catalysts. The synthesized $Ni_2(NDISA)$ -PDA-Pd exhibits high catalytic activity for Suzuki coupling reactions, particularly when compared to the parent MOF containing Pd NPs, $Ni_2(NDISA)$ -Pd. Thus, the reported method not only is a very promising approach for preserving or inducing permanent porosity and high surface areas in large-pore structures but could be used to further optimize MOFs for many applications related to separations, gas and liquid phase catalysis, etc.

EXPERIMENTAL SECTION

Materials. Free-base dopamine was synthesized according to our previous report.⁴³ Naphthalene-1,4,5,8-tetracarboxylic dianhydride (>97.0%) was provided by TCL. 5-Amino-2-hydroxybenzoic acid was supplied by Merck. $Ni(NO_3)_2 \cdot 6H_2O$ (98%) and $Co(NO_3)_2 \cdot 6H_2O$ (99%) were purchased from ABCR. $Mg(NO_3)_2 \cdot 6H_2O$ (99%) and $Zn(NO_3)_2 \cdot 6H_2O$ (98%) were purchased from Sigma.

Ligand H_4NDISA Synthesis. Naphthalene-1,4,5,8-tetracarboxylic dianhydride (9.97 g, 37.2 mmol) and 5-amino-2-hydroxybenzoic acid (11.72 g, 76.5 mmol) were dissolved in anhydrous dimethylformamide (DMF) (350 mL) under nitrogen and heated at 130 °C while stirred vigorously for 24 h. The mixture was then cooled to room temperature, and the resulting orange suspension was filtered, washed with DMF, diethyl ether, and methanol, and then dried under vacuum to yield an orange powder. Purification of the crude product was performed by washing it with 2 M HCl (100 mL) for 1 day. Analytical data matched previously reported values.

$Ni_2(NDISA)$ Synthesis. $Ni(NO_3)_2 \cdot 6H_2O$ (104 mg) was mixed with H_4NDISA (55 mg) in a solvent mixture (DMF/ $C_2H_5OH/H_2O = 7.5$ mL:0.5 mL:0.5 mL) in a 16 mL glass vial with a Teflon-sealed cap. The vial with the reaction mixture was ultrasonicated for 15 min and then seated in the oven at 120 °C for 24 h. After cooling, the product was washed with DMF twice and methanol twice.

$Co_2(NDISA)$ Synthesis. $Co(NO_3)_2 \cdot 6H_2O$ (104 mg) was mixed with H_4NDISA (55 mg) in a solvent mixture (DMF/ $C_2H_5OH/H_2O = 7.5$ mL:0.5 mL:0.5 mL) in a 16 mL glass vial with a Teflon-sealed cap. The vial with the reaction mixture was ultrasonicated for 15 min and then seated in the oven at 120 °C for 24 h. After cooling, the product was washed with DMF twice and methanol twice.

$Mg_2(NDISA)$ Synthesis. $Mg(NO_3)_2 \cdot 6H_2O$ (80 mg) was mixed with H_4NDISA (55 mg) in a solvent mixture (DMF/ $C_2H_5OH/H_2O = 7.5$ mL:0.5 mL:0.5 mL) in a 16 mL glass vial with a Teflon-sealed cap. The vial with the reaction mixture was ultrasonicated for 15 min then seated in an oven at 120 °C for 24 h. After cooling, the product was washed with DMF twice and methanol twice.

$Zn_2(NDISA)$ Synthesis. $Zn(NO_3)_2 \cdot 6H_2O$ (107 mg) was mixed with H_4NDISA (55 mg) in a solvent mixture (DMF/ $C_2H_5OH = 7.5$ mL:0.5 mL) in a 16 mL glass vial with a Teflon-sealed cap. The vial with the reaction mixture was ultrasonicated for 15 min and then seated in an oven at 120 °C for 24 h. After cooling, the product was washed with DMF twice and methanol twice.

$M_2(NDISA)$ -PDA ($M = Ni, Co, Mg, Zn$) Synthesis. $M_2(NDISA)$ (100 mg) was dispersed in 15 mL of methanol in a 50 mL round-bottom flask and sonicated for 5 min. A desired amount of free-base dopamine was dissolved in 5 mL of methanol; then this dopamine methanol solution was added into the flask and mixed with $M_2(NDISA)$. (See detailed information in Table S2.) The mixture was stirred at room temperature for 12 h (using a needle to connect with air). After the reaction finished, the product was centrifuged and washed with methanol once.

$M_2(\text{NDISA})\text{-PEI}$ ($M = \text{Ni, Co, Mg, Zn}$) *Synthesis*. A desired amount of PEI (25 mg) was added to 4 mL of methanol and sonicated, and then this was added to $M_2(\text{NDISA})$ (100 mg) which was dispersed in 8 mL of methanol. After stirring at room temperature for 6 h, the samples were washed with methanol once and dried.

$\text{Ni}_2(\text{NDISA})\text{-PDA-Pd}$ *Synthesis*. In a 50 mL flask, 100 mg of $\text{Ni}_2(\text{NDISA})$ MOF was dispersed in 15 mL of methanol with the help of ultrasound. Then 25 mg of free-base dopamine in 5 mL of methanol was added into the MOF suspension. After 12 h of polymerization, the product was centrifuged and washed with methanol one time. The recovered solid was redispersed in 40 mL of methanol, and 620 μL of a 0.0564 mol/L $\text{Pd}(\text{NO}_3)_2$ aqueous solution was added dropwise. After stirring for 5.5 h, the $\text{Ni}_2(\text{NDISA})\text{-PDA-Pd}$ catalyst was recovered and washed with methanol three times and dried in a vacuum oven at room temperature.

$\text{Ni}_2(\text{NDISA})\text{-Pd}$ *Synthesis*. In a 50 mL flask, 100 mg of $\text{Ni}_2(\text{NDISA})$ MOF was dispersed in 40 mL of methanol with the help of ultrasound. Then 620 μL of a 0.0564 mol/L $\text{Pd}(\text{NO}_3)_2$ aqueous solution was added dropwise. After stirring for 5.5 h, the $\text{Ni}_2(\text{NDISA})\text{-Pd}$ catalyst was recovered and washed with methanol three times and dried in a vacuum oven at room temperature.

PDA-Pd Synthesis. A 180 mg amount of free-base dopamine was dispersed in 25 mL of methanol; then the solution was stirred under an oxygen atmosphere for 12 h. Later, the black product was recovered and washed with MeOH three times. After drying for 8 h under vacuum at room temperature, the PDA sample was obtained. Then 70 mg of PDA was dispersed in 28 mL of methanol under ultrasound; later 435 μL of a $\text{Pd}(\text{NO}_3)_2$ (0.0564 mol/L) aqueous solution was added dropwise. After stirring for 5.5 h, the product was centrifuged and washed with MeOH three times. Finally, the collected product PDA-Pd was dried under vacuum for 8 h at room temperature for further use. ICP-OES analysis revealed the Pd loading is 3.27 wt % in PDA-Pd.

General Procedure for Suzuki–Miyaura Cross-Coupling Reaction. In a reaction tube, aryl halide (1.0 mmol), phenylboronic acid (1.1 mmol), K_2CO_3 (1.5 mmol), and $\text{Ni}_2(\text{NDISA})\text{-PDA-Pd}$ (0.1 mol % Pd loading) were added into a DMF/ H_2O (3 mL, $V_{\text{DMF}}:V_{\text{H}_2\text{O}} = 1:1$) mixed solution. Then, the tube was put into a preheated 50 °C oil bath for the desired reaction time. When the reaction time was reached, the reaction solution was cooled to room temperature and 5 mL of ethyl acetate and 105 μL of *n*-dodecane (internal standard) were added. The solution was centrifuged to remove solids, and the organic solution was analyzed by a gas chromatograph (Agilent 7890B) equipped with a flame ionization detector, an MS detector (5977A), and an HP-5 ms capillary column (0.25 mm in diameter, 30 m in length).

Characterization. The XRD patterns were obtained on a Bruker D8 diffractometer with Cu $K\alpha$ radiation ($\lambda = 1.5418 \text{ \AA}$) at 40 kV and 40 mA. The morphology and microstructures of the samples were characterized by scanning electron microscopy (FEI Teneo) and transmission electron microscopy (FEI Tecnai G2 Spirit Twin). High-angle annular dark-field (HAADF) imaging was performed on a FEI Osiris in scanning transmission electron microscopy mode (STEM) at an accelerating voltage of 200 kV. XPS measurement was performed using a Physical Instruments AG PHI VersaProbe II scanning XPS microprobe. Analysis was performed using a monochromatic Al $K\alpha$ X-ray source of 24.8 W power with a beam size of 100 μm . Nitrogen adsorption–desorption isotherms were obtained on a BELSORP-max instrument at 77 K. The metal contents in the samples were measured on an Agilent 5110 Synchronous Vertical Dual View ICP-OES.

Molecular Simulation. Molecular dynamics simulations in the canonical (NVT) ensemble were used to calculate forces and torques on the metal helices of the $M_2(\text{NDISA})$ and $M_2(\text{NDISA})\text{-PDA}$ frameworks. The MOF unit cell was replicated six times in the *c* direction and three times in both the *a* and *b* directions to make the simulation box. Simulations were 2 ns long, and force data were stored every 20 fs. Only the last 50% of data was used for data analysis. Simulations were run with a time step of 1 fs with a Nosé–Hoover thermostat at a temperature of 300 K in the LAMMPS

molecular software package.^{51,67} Both bonded and nonbonded interactions between ligand atoms are taken from the DREIDING force field⁶⁸ as implemented in LAMMPS Interface.⁶⁹ To make sure the DREIDING force field is correctly modeling the ground state configuration of the ligands, we compared the geometry-optimized structure of the ligand with the force field with density functional theory (DFT). The DFT calculations were carried out with TeraChem⁷⁰ at the B3LYP⁷¹ level of theory and 6-31G* basis. The force field correctly found the ground state configuration of the ligand. Metal–metal and metal–oxygen interactions are taken from a model for $M_2(\text{dobdc})$ analogues.⁵⁰ Geometric mixing rules are used to combine DREIDING Lennard-Jones parameters for carbon and hydrogen with the $M_2(\text{dobdc})$ model-based metal–metal interactions to compute the nonbonded metal–carbon and metal–hydrogen interactions. Nonbonded and short-range electrostatic interactions were truncated at 12.5 Å , and Ewald summations were used to calculate long-range electrostatic interactions. EReq charges were used for $M_2(\text{NDISA})$ atoms.^{72,73} The PDA dimer atoms were modeled without charges.

■ ASSOCIATED CONTENT

📄 Supporting Information

The Supporting Information is available free of charge on the ACS Publications website at DOI: 10.1021/jacs.9b05967.

Supporting figures and tables, SEM and TEM images, powder X-ray diffraction patterns, TGA analysis, Le Bail fits, *in situ* DRIFTS, CO_2 adsorption isotherms, isosteric heat of CO_2 adsorption, N_2 adsorption isotherms, pore size distributions, XPS spectrum (PDF)

■ AUTHOR INFORMATION

Corresponding Author

*wendy.queen@epfl.ch

ORCID

Sudi Jawahery: 0000-0001-9950-6199

Seyed Mohamad Moosavi: 0000-0002-0357-5729

Mohammad Khaja Nazeeruddin: 0000-0001-5955-4786

Berend Smit: 0000-0003-4653-8562

Wendy L. Queen: 0000-0002-8375-2341

Author Contributions

[#]L.P. and S.Y. contributed equally to this work.

Notes

The authors declare no competing financial interest.

■ ACKNOWLEDGMENTS

This work was supported by the Swiss National Science Foundation under grant PYAPP2_160581. M.A. is financially supported by the Swiss Commission for Technology and Innovation (CTI). S.J. was supported as part of the Center for Gas Separations Relevant to Clean Energy Technologies, an Energy Frontier Research Center funded by the U.S. Department of Energy, Office of Science, Basic Energy Sciences, under Award DE-SC0001015. S.J. acknowledges support from an NSF Graduate Research Fellowship. S.M.M. acknowledges support from the Swiss National Science Foundation under fellowship award P1ELP2_184404. The authors also gratefully thank N. Gasilova and Daniel T. Sun for the help with MALDI-TOF.

■ REFERENCES

(1) Furukawa, H.; Cordova, K. E.; O’Keeffe, M.; Yaghi, O. M. The Chemistry and Applications of Metal–Organic Frameworks. *Science* 2013, 341, 1230444.

- (2) Zhou, H.-C. J.; Kitagawa, S. Metal-Organic Frameworks (MOFs). *Chem. Soc. Rev.* **2014**, *43*, 5415–5418.
- (3) Cohen, S. M. The Postsynthetic Renaissance in Porous Solids. *J. Am. Chem. Soc.* **2017**, *139*, 2855–2863.
- (4) Hönicke, I. M.; Senkovska, I.; Bon, V.; Baburin, I. A.; Bönisch, N.; Raschke, S.; Evans, J. D.; Kaskel, S. Balancing Mechanical Stability and Ultrahigh Porosity in Crystalline Framework Materials. *Angew. Chem., Int. Ed.* **2018**, *57*, 13780–13783.
- (5) Stassen, I.; Burtch, N.; Talin, A.; Falcaro, P.; Allendorf, M.; Ameloot, R. An Updated Roadmap for the Integration of Metal-Organic Frameworks with Electronic Devices and Chemical Sensors. *Chem. Soc. Rev.* **2017**, *46*, 3185–3241.
- (6) Queen, W. L.; Hudson, M. R.; Bloch, E. D.; Mason, J. A.; Gonzalez, M. I.; Lee, J. S.; Gygi, D.; Howe, J. D.; Lee, K.; Darwish, T. A.; James, M.; Peterson, V. K.; Teat, S. J.; Smit, B.; Neaton, J. B.; Long, J. R.; Brown, C. M. Comprehensive Study of Carbon Dioxide Adsorption in the Metal-Organic Frameworks $M_2(\text{dobdc})$ ($M = \text{Mg}, \text{Mn}, \text{Fe}, \text{Co}, \text{Ni}, \text{Cu}, \text{Zn}$). *Chem. Sci.* **2014**, *5*, 4569–4581.
- (7) Stassen, I.; Styles, M.; Greci, G.; Gorp, H. V.; Vanderlinden, W.; Feyter, S. D.; Falcaro, P.; Vos, D. D.; Vereecken, P.; Ameloot, R. Chemical Vapour Deposition of Zeolitic Imidazolate Framework Thin Films. *Nat. Mater.* **2016**, *15*, 304–310.
- (8) DeCoste, J. B.; Denny, J. M. S.; Peterson, G. W.; Mahle, J. J.; Cohen, S. M. Enhanced Aging Properties of HKUST-1 in Hydrophobic Mixed-Matrix Membranes for Ammonia Adsorption. *Chem. Sci.* **2016**, *7*, 2711–2716.
- (9) Horcajada, P.; Serre, C.; Vallet-Regí, M.; Sebban, M.; Taulelle, F.; Férey, G. Metal-Organic Frameworks as Efficient Materials for Drug Delivery. *Angew. Chem., Int. Ed.* **2006**, *45*, 5974–5978.
- (10) Mondloch, J. E.; Katz, M. J.; Isley, W. C.; Iii, Ghosh, P.; Liao, P.; Bury, W.; Wagner, G. W.; Hall, M. G.; DeCoste, J. B.; Peterson, G. W.; Snurr, R. Q.; Cramer, C. J.; Hupp, J. T.; Farha, O. K. Destruction of Chemical Warfare Agents Using Metal-Organic Frameworks. *Nat. Mater.* **2015**, *14*, 512–516.
- (11) Dang, S.; Zhu, Q.-L.; Xu, Q. Nanomaterials Derived from Metal-Organic Frameworks. *Nat. Rev. Mater.* **2018**, *3*, 17075.
- (12) Sun, L.; Campbell, M. G.; Dincă, M. Electrically Conductive Porous Metal-Organic Frameworks. *Angew. Chem., Int. Ed.* **2016**, *55*, 3566–3579.
- (13) Yue, Y.; Fulvio, P. F.; Dai, S. Hierarchical Metal-Organic Framework Hybrids: Perturbation-Assisted Nanofusion Synthesis. *Acc. Chem. Res.* **2015**, *48*, 3044–3052.
- (14) Tsumori, N.; Chen, L.; Wang, Q.; Zhu, Q.-L.; Kitta, M.; Xu, Q. Quasi-MOF: Exposing Inorganic Nodes to Guest Metal Nanoparticles for Drastically Enhanced Catalytic Activity. *Chem.* **2018**, *4*, 845–856.
- (15) Tan, Y. C.; Zeng, H. C. Defect Creation in HKUST-1 via Molecular Imprinting: Attaining Anionic Framework Property and Mesoporosity for Cation Exchange Applications. *Adv. Funct. Mater.* **2017**, *27*, 1703765.
- (16) Guan, H.-Y.; LeBlanc, R. J.; Xie, S.-Y.; Yue, Y. Recent Progress in the Syntheses of Mesoporous Metal-Organic Framework Materials. *Coord. Chem. Rev.* **2018**, *369*, 76–90.
- (17) Peng, L.; Zhang, J.; Xue, Z.; Han, B.; Sang, X.; Liu, C.; Yang, G. Highly Mesoporous Metal-Organic Framework Assembled in a Switchable Solvent. *Nat. Commun.* **2014**, *5*, 5465.
- (18) Liu, W.; Huang, J.; Yang, Q.; Wang, S.; Sun, X.; Zhang, W.; Liu, J.; Huo, F. Multi-Shelled Hollow Metal-Organic Frameworks. *Angew. Chem., Int. Ed.* **2017**, *56*, 5512–5516.
- (19) Deng, H.; Grunder, S.; Cordova, K. E.; Valente, C.; Furukawa, H.; Hmadeh, M.; Gandara, F.; Whalley, A. C.; Liu, Z.; Asahina, S.; Kazumori, H.; O’Keefe, M.; Terasaki, O.; Stoddart, J. F.; Yaghi, O. M. Large-Pore Apertures in a Series of Metal-Organic Frameworks. *Science* **2012**, *336*, 1018–1023.
- (20) AlKaabi, K.; Wade, C. R.; Dincă, M. Transparent-to-Dark Electrochromic Behavior in Naphthalene-Diimide-Based Mesoporous MOF-74 Analogs. *Chem.* **2016**, *1*, 264–272.
- (21) Xuan, W.; Zhu, C.; Liu, Y.; Cui, Y. Mesoporous Metal–Organic Framework Materials. *Chem. Soc. Rev.* **2012**, *41*, 1677–1695.
- (22) Souto, M.; Santiago-Portillo, A.; Palomino, M.; Vitorica-Yrzebal, I.; Vieira, B. J. C.; Waerenborgh, J. C. C.; Valencia, S.; Navalon, S.; Rey, F.; Garcia, H.; Minguez Espallargas, G. A Highly Stable and Hierarchical Tetrathiafulvalene-based Metal-Organic Framework with Improved Performance as Solid Catalyst. *Chem. Sci.* **2018**, *9*, 2413–2418.
- (23) Towsif Abtab, S. M.; Alezi, D.; Bhatt, P. M.; Shkurenko, A.; Belmabkhout, Y.; Aggarwal, H.; Weseliński, Ł. J.; Alsadun, N.; Samin, U.; Hedhili, M. N.; Eddaoudi, M. Reticular Chemistry in Action: A Hydrolytically Stable MOF Capturing Twice Its Weight in Adsorbed Water. *Chem.* **2018**, *4*, 94–105.
- (24) Nelson, A. P.; Farha, O. K.; Mulfort, K. L.; Hupp, J. T. Supercritical Processing as a Route to High Internal Surface Areas and Permanent Microporosity in Metal-Organic Framework Materials. *J. Am. Chem. Soc.* **2009**, *131*, 458–460.
- (25) Ma, L.; Jin, A.; Xie, Z.; Lin, W. Freeze Drying Significantly Increases Permanent Porosity and Hydrogen Uptake in 4,4-Connected Metal-Organic Frameworks. *Angew. Chem., Int. Ed.* **2009**, *48*, 9905–9908.
- (26) Ma, L.; Falkowski, J. M.; Abney, C.; Lin, W. A Series of Isoreticular Chiral Metal-Organic Frameworks as a Tunable Platform for Asymmetric Catalysis. *Nat. Chem.* **2010**, *2*, 838–846.
- (27) Park, Y. K.; Choi, S. B.; Kim, H.; Kim, K.; Won, B.-H.; Choi, K.; Choi, J.-S.; Ahn, W.-S.; Won, N.; Kim, S.; Jung, D. H.; Choi, S.-H.; Kim, G.-H.; Cha, S.-S.; Jhon, Y. H.; Yang, J. K.; Kim, J. Crystal Structure and Guest Uptake of a Mesoporous Metal-Organic Framework Containing Cages of 3.9 and 4.7 nm in Diameter. *Angew. Chem., Int. Ed.* **2007**, *46*, 8230–8233.
- (28) Mondloch, J. E.; Karagiari, O.; Farha, O. K.; Hupp, J. T. Activation of Metal-Organic Framework Materials. *CrystEngComm* **2013**, *15*, 9258–9264.
- (29) Moosavi, S. M.; Boyd, P. G.; Sarkisov, L.; Smit, B. Improving the Mechanical Stability of Metal-Organic Frameworks Using Chemical Caryatids. *ACS Cent. Sci.* **2018**, *4*, 832–839.
- (30) Howarth, A. J.; Liu, Y.; Li, P.; Li, Z.; Wang, T. C.; Hupp, J. T.; Farha, O. K. Chemical, Thermal and Mechanical Stabilities of Metal-Organic Frameworks. *Nat. Rev. Mater.* **2016**, *1*, 15018.
- (31) Wenzel, S. E.; Fischer, M.; Hoffmann, F.; Fröba, M. Highly Porous Metal-Organic Framework Containing a Novel Organosilicon Linker - A Promising Material for Hydrogen Storage. *Inorg. Chem.* **2009**, *48*, 6559–6565.
- (32) Zhuang, W.; Ma, S.; Wang, X.-S.; Yuan, D.; Li, J.-R.; Zhao, D.; Zhou, H.-C. Introduction of Cavities up to 4 nm into a Hierarchically-Assembled Metal-Organic Framework Using an Angular, Tetratopic Ligand. *Chem. Commun.* **2010**, *46*, 5223–5225.
- (33) Meek, S. T.; Perry, J. J.; Teich-McGoldrick, S. L.; Greathouse, J. A.; Allendorf, M. D. Complete Series of Monohalogenated Isoreticular Metal-Organic Frameworks: Synthesis and the Importance of Activation Method. *Cryst. Growth Des.* **2011**, *11*, 4309–4312.
- (34) Mondal, S. S.; Bhunia, A.; Attallah, A. G.; Matthes, P. R.; Kelling, A.; Schilde, U.; Müller-Buschbaum, K.; Krause-Rehberg, R.; Janiak, C.; Holdt, H.-J. Study of the Discrepancies between Crystallographic Porosity and Guest Access into Cadmium-Imidazolate Frameworks and Tunable Luminescence Properties by Incorporation of Lanthanides. *Chem. - Eur. J.* **2016**, *22*, 6905–6913.
- (35) Yang, J.; Wang, X.; Dai, F.; Zhang, L.; Wang, R.; Sun, D. Improving the Porosity and Catalytic Capacity of a Zinc Paddlewheel Metal-Organic Framework (MOF) through Metal-Ion Metathesis in a Single-Crystal-to-Single-Crystal Fashion. *Inorg. Chem.* **2014**, *53*, 10649–10653.
- (36) Feldblyum, J. I.; Liu, M.; Gidley, D. W.; Matzger, A. J. Reconciling the Discrepancies between Crystallographic Porosity and Guest Access as Exemplified by Zn-HKUST-1. *J. Am. Chem. Soc.* **2011**, *133*, 18257–18263.
- (37) Dodson, R. A.; Wong-Foy, A. G.; Matzger, A. J. The Metal-Organic Framework Collapse Continuum: Insights from Two-Dimensional Powder X-ray Diffraction. *Chem. Mater.* **2018**, *30*, 6559–6565.

- (38) Willems, T. F.; Rycroft, C. H.; Kazi, M.; Meza, J. C.; Haranczyk, M. Algorithms and Tools for High-Throughput Geometry-Based Analysis of Crystalline Porous Materials. *Micro-porous Mesoporous Mater.* **2012**, *149*, 134–141.
- (39) Kitao, T.; Zhang, Y.; Kitagawa, S.; Wang, B.; Uemura, T. Hybridization of MOFs and Polymers. *Chem. Soc. Rev.* **2017**, *46*, 3108–3133.
- (40) Le Ouay, B.; Uemura, T. Polymer in MOF Nanospace: from Controlled Chain Assembly to New Functional Materials. *Isr. J. Chem.* **2018**, *58*, 995–1009.
- (41) Iizuka, T.; Honjo, K.; Uemura, T. Enhanced Mechanical Properties of a Metal-Organic Framework by Polymer Insertion. *Chem. Commun.* **2019**, *55*, 691–694.
- (42) Le Ouay, B.; Kitagawa, S.; Uemura, T. Opening of an Accessible Microporosity in an Otherwise Nonporous Metal-Organic Framework by Polymeric Guests. *J. Am. Chem. Soc.* **2017**, *139*, 7886–7892.
- (43) Sun, D. T.; Peng, L.; Reeder, W. S.; Moosavi, S. M.; Tiana, D.; Britt, D. K.; Oveisi, E.; Queen, W. L. Rapid, Selective Heavy Metal Removal from Water by a Metal-Organic Framework/Polydopamine Composite. *ACS Cent. Sci.* **2018**, *4*, 349–356.
- (44) Bloch, E. D.; Hudson, M. R.; Mason, J. A.; Chavan, S.; Crocellà, V.; Howe, J. D.; Lee, K.; Dzubak, A. L.; Queen, W. L.; Zadrozny, J. M.; Geier, S. J.; Lin, L.-C.; Gagliardi, L.; Smit, B.; Neaton, J. B.; Bordiga, S.; Brown, C. M.; Long, J. R. Reversible CO Binding Enables Tunable CO/H₂ and CO/N₂ Separations in Metal-Organic Frameworks with Exposed Divalent Metal Cations. *J. Am. Chem. Soc.* **2014**, *136*, 10752–10761.
- (45) Peng, L.; Asgari, M.; Mievil, P.; Schouwink, P.; Bulut, S.; Sun, D. T.; Zhou, Z.; Pattison, P.; van Beek, W.; Queen, W. L. Using Predefined M₃(μ₃-O) Clusters as Building Blocks for an Isostructural Series of Metal-Organic Frameworks. *ACS Appl. Mater. Interfaces* **2017**, *9*, 23957–23966.
- (46) Kong, X.; Scott, E.; Ding, W.; Mason, J. A.; Long, J. R.; Reimer, J. A. CO₂ Dynamics in a Metal-Organic Framework with Open Metal Sites. *J. Am. Chem. Soc.* **2012**, *134*, 14341–14344.
- (47) McDonald, T. M.; Lee, W. R.; Mason, J. A.; Wiers, B. M.; Hong, C. S.; Long, J. R. Capture of Carbon Dioxide from Air and Flue Gas in the Alkylamine-Appended Metal-Organic Framework mmen-Mg₂(dobpdc). *J. Am. Chem. Soc.* **2012**, *134*, 7056–7065.
- (48) Liu, Y.; Kabbour, H.; Brown, C. M.; Neumann, D. A.; Ahn, C. C. Increasing the Density of Adsorbed Hydrogen with Coordinatively Unsaturated Metal Centers in Metal-Organic Frameworks. *Langmuir* **2008**, *24*, 4772–4777.
- (49) Xiao, D. J.; Bloch, E. D.; Mason, J. A.; Queen, W. L.; Hudson, M. R.; Planas, N.; Borycz, J.; Dzubak, A. L.; Verma, P.; Lee, K.; Bonino, F.; Crocellà, V.; Yano, J.; Bordiga, S.; Truhlar, D. G.; Gagliardi, L.; Brown, C. M.; Long, J. R. Oxidation of Ethane to Ethanol by N₂O in a Metal-Organic Framework with Coordinatively Unsaturated Iron(II) Sites. *Nat. Chem.* **2014**, *6*, 590–595.
- (50) Jawahery, S.; Rampal, N.; Moosavi, S. M.; Witman, M.; Smit, B. Ab Initio Flexible Force Field for Metal-Organic Frameworks Using Dummy Model Coordination Bonds. *J. Chem. Theory Comput.* **2019**, *15*, 3666–3677.
- (51) Plimpton, S. Fast Parallel Algorithms for Short-Range Molecular Dynamics. *J. Comput. Phys.* **1995**, *117*, 1–19.
- (52) Roque-Malherbe, R. *Adsorption and Diffusion in Nanoporous Materials*; CRC Press: Boca Raton, 2007.
- (53) McDonald, T. M.; Mason, J. A.; Kong, X.; Bloch, E. D.; Gygi, D.; Dani, A.; Crocellà, V.; Giordanino, F.; Odoh, S. O.; Drisdell, W. S.; Vlasisavljevich, B.; Dzubak, A. L.; Poloni, R.; Schnell, S. K.; Planas, N.; Lee, K.; Pascal, T.; Wan, L. F.; Prendergast, D.; Neaton, J. B.; Smit, B.; Kortright, J. B.; Gagliardi, L.; Bordiga, S.; Reimer, J. A.; Long, J. R. Cooperative Insertion of CO₂ in Diamine-Appended Metal-Organic Frameworks. *Nature* **2015**, *519*, 303–308.
- (54) Peng, L.; Yang, S.; Sun, D. T.; Asgari, M.; Queen, W. L. MOF/Polymer Composite Synthesized using a Double Solvent Method Offers Enhanced Water and CO₂ Adsorption Properties. *Chem. Commun.* **2018**, *54*, 10602–10605.
- (55) Aliev, S. B.; Samsonenko, D. G.; Maksimovskiy, E. A.; Fedorovskaya, E. O.; Sapchenko, S. A.; Fedin, V. P. Polyaniline-intercalated MIL-101: Selective CO₂ Sorption and Supercapacitor Properties. *New J. Chem.* **2016**, *40*, 5306–5312.
- (56) Zhu, Q.-L.; Li, J.; Xu, Q. Immobilizing Metal Nanoparticles to Metal-Organic Frameworks with Size and Location Control for Optimizing Catalytic Performance. *J. Am. Chem. Soc.* **2013**, *135*, 10210–10213.
- (57) Yang, Q.; Chen, Y.-Z.; Wang, Z. U.; Xu, Q.; Jiang, H.-L. One-Pot Tandem Catalysis over Pd@MIL-101: Boosting the Efficiency of Nitro Compound Hydrogenation by Coupling with Ammonia Borane Dehydrogenation. *Chem. Commun.* **2015**, *51*, 10419–10422.
- (58) Chen, Y.-Z.; Xu, Q.; Yu, S.-H.; Jiang, H.-L. Tiny Pd@Co Core-Shell Nanoparticles Confined inside a Metal-Organic Framework for Highly Efficient Catalysis. *Small* **2015**, *11*, 71–76.
- (59) Chen, Y.-Z.; Zhou, Y.-X.; Wang, H.; Lu, J.; Uchida, T.; Xu, Q.; Yu, S.-H.; Jiang, H.-L. Multifunctional PdAg@MIL-101 for One-Pot Cascade Reactions: Combination of Host-Guest Cooperation and Bimetallic Synergy in Catalysis. *ACS Catal.* **2015**, *5*, 2062–2069.
- (60) Lu, S.; Hu, Y.; Wan, S.; McCaffrey, R.; Jin, Y.; Gu, H.; Zhang, W. Synthesis of Ultrafine and Highly Dispersed Metal Nanoparticles Confined in a Thioether-Containing Covalent Organic Framework and Their Catalytic Applications. *J. Am. Chem. Soc.* **2017**, *139*, 17082–17088.
- (61) Yang, S.; Peng, L.; Bulut, S.; Queen, W. L. Recent Advances of MOFs and MOF-Derived Materials in Thermally-Driven Organic Transformations. *Chem. - Eur. J.* **2019**, *25*, 2161–2178.
- (62) Shen, K.; Zhang, L.; Chen, X.; Liu, L.; Zhang, D.; Han, Y.; Chen, J.; Long, J.; Luque, R.; Li, Y.; Chen, B. Ordered Macroporous Metal-Organic Framework Single Crystals. *Science* **2018**, *359*, 206–210.
- (63) Fihri, A.; Bouhrara, M.; Nekoueshahraki, B.; Basset, J.-M.; Polshettiwar, V. Nanocatalysts for Suzuki Cross-Coupling Reactions. *Chem. Soc. Rev.* **2011**, *40*, 5181–5203.
- (64) Chen, X.; Wu, G.; Chen, J.; Chen, X.; Xie, Z.; Wang, X. Synthesis of “Clean” and Well-Dispersive Pd Nanoparticles with Excellent Electrocatalytic Property on Graphene Oxide. *J. Am. Chem. Soc.* **2011**, *133*, 3693–3695.
- (65) Cargnello, M.; Chen, C.; Diroll, B. T.; Doan-Nguyen, V. V. T.; Gorte, R. J.; Murray, C. B. Efficient Removal of Organic Ligands from Supported Nanocrystals by Fast Thermal Annealing Enables Catalytic Studies on Well-Defined Active Phases. *J. Am. Chem. Soc.* **2015**, *137*, 6906–6911.
- (66) Yang, S.; Peng, L.; Sun, D. T.; Asgari, M.; Oveisi, E.; Trukhina, O.; Bulut, S.; Jamali, A.; Queen, W. L. A New Post-Synthetic Polymerization Strategy Makes Metal-Organic Frameworks More Stable. *Chem. Sci.* **2019**, *10*, 4542–4549.
- (67) Braun, E.; Moosavi, S. M.; Smit, B. Anomalous Effects of Velocity Rescaling Algorithms: The Flying Ice Cube Effect Revisited. *J. Chem. Theory Comput.* **2018**, *14*, 5262–5272.
- (68) Mayo, S. L.; Olafson, B. D.; Goddard, W. A. DREIDING: a Generic Force Field for Molecular Simulations. *J. Phys. Chem.* **1990**, *94*, 8897–8909.
- (69) Boyd, P. G.; Moosavi, S. M.; Witman, M.; Smit, B. Force-Field Prediction of Materials Properties in Metal-Organic Frameworks. *J. Phys. Chem. Lett.* **2017**, *8*, 357–363.
- (70) Ufimtsev, I. S.; Martinez, T. J. Quantum Chemistry on Graphical Processing Units. 3. Analytical Energy Gradients, Geometry Optimization, and First Principles Molecular Dynamics. *J. Chem. Theory Comput.* **2009**, *5*, 2619–2628.
- (71) Becke, A. D. Density-functional Thermochemistry. III. The Role of Exact Exchange. *J. Chem. Phys.* **1993**, *98*, 5648–5652.
- (72) Wilmer, C. E.; Kim, K. C.; Snurr, R. Q. An Extended Charge Equilibration Method. *J. Phys. Chem. Lett.* **2012**, *3*, 2506–2511.
- (73) Ongari, D.; Boyd, P. G.; Kadioglu, O.; Mace, A. K.; Keskin, S.; Smit, B. Evaluating Charge Equilibration Methods to Generate Electrostatic Fields in Nanoporous Materials. *J. Chem. Theory Comput.* **2019**, *15*, 382–401.